physica status solidi a
www.pss-a.com

Weak Frequency Dispersion of *C–V* Characteristics of AlGaN/GaN Metal-Insulator-Semiconductor Devices Despite High Interface Trap Density

Yuchen Deng, Jieensi Gelan, Kazuya Uryu, and Toshi-kazu Suzuki*

For AlGaN/GaN metal-insulator-semiconductor (MIS) devices, it is shown that there is a case where the frequency dispersion of the capacitance–voltage (*C–V*) characteristics is very weak despite a rather high insulator–semiconductor interface trap density. We fabricated metal/Al_2O_3/AlGaN/GaN MIS devices, and carried out *C–V* characterization of them. Although they exhibit very weak *C–V* frequency dispersion for 100 Hz–1 MHz, we found that, based on the conductance method, the insulator–semiconductor interface trap densities are rather high $\approx 3 \times 10^{13}\,cm^{-2}\,eV^{-1}$. As a possible explanation, a double-peak model is considered, which underlines the possibility that a high interface trap density does not necessarily lead to strong *C–V* frequency dispersion. The model can explain the observed weak *C–V* frequency dispersion, implying that it is not appropriate to naively discuss the interface traps only from the apparent *C–V* frequency dispersion.

1. Introduction

GaN-based metal-insulator-semiconductor (MIS) devices have been extensively investigated, owing to the merit of gate leakage reduction. As a gate insulator, various materials have been employed and studied, such as Al_2O_3,[1] AlTiO,[2–8] AlSiO,[9,10] HfO_2,[11,12] TiO_2,[13] TaON,[14] AlON,[15] AlN,[16–20] and BN.[21,22] In any cases, the insulator–semiconductor interface properties are quite important. Since the threshold voltage is strongly affected by insulator–semiconductor interface fixed charges, interface charge engineering[23,24] has been explored.[6,7,25–27] Moreover, device instability caused by insulator–semiconductor interface traps is a critical issue.[28] The interface traps significantly depend on the device fabrication processes and have been extensively investigated by several methods. In particular, the conductance method[29–31] is a very strong tool, where the conductance (the real part of the trap admittance) is analyzed as a function of frequency, and the trap density can be obtained as well as the trapping time constant. In many cases, strong frequency dispersion of the capacitance-voltage (*C–V*) characteristics is associated with a high interface trap density, while weak *C–V* frequency dispersion is associated with a low interface trap density.[32,33] This is natural because the capacitance, which is obtained from the imaginary part of the trap admittance, is closely related to the conductance (the real part). Thus, in many cases, a low interface trap density is inferred when the *C–V* frequency dispersion is weak.[34] However, this is not always true; apparent weak frequency dispersion is not always associated with a low interface trap density.[35,36] Therefore, there are uncertainties in discussing the interface trap density just based on the apparent *C–V* frequency dispersion.

In this article, we shed light on the relation between the insulator–semiconductor interface trap density and the apparent *C–V* frequency dispersion for metal/Al_2O_3/AlGaN/GaN MIS capacitor devices. First, we show that, although the devices exhibit very weak *C–V* frequency dispersion for 100 Hz-1 MHz, the insulator–semiconductor interface trap densities obtained by the conductance method are rather high $\approx 3 \times 10^{13}\,cm^{-2}\,eV^{-1}$. Next, we consider a double-peak model to explain this, showing the possibility that a high interface trap density does not necessarily lead to strong *C–V* frequency dispersion. We should note that it is not appropriate to naively discuss the interface traps only from the apparent *C–V* frequency dispersion.

2. Device Fabrication and Characterization

Using an $Al_{0.24}Ga_{0.76}N$ (20 nm)/GaN (3 μm) heterostructure grown by metal–organic vapor phase epitaxy on a sapphire (0001) substrate, we fabricated metal/Al_2O_3/AlGaN/GaN MIS capacitor devices with a gate area of $75^2\,\mu m^2$, whose schematic is shown in **Figure 1**a. Ti-based Ohmic electrodes were formed, using Ti (5 nm)/Al (200 nm)/Ti (100 nm)/Au (50 nm) annealed at 575 °C in N_2 ambient. The Ohmic contact resistance of $\approx 1\,\Omega\,mm$ was confirmed by transfer length method measurements. After that, several thicknesses of Al_2O_3 gate insulators were formed by atomic layer deposition at 150 °C, using

Y. Deng, J. Gelan, T. Suzuki
Center for Nano Materials and Technology
Japan Advanced Institute of Science and Technology (JAIST)
1-1 Asahidai, Nomi, Ishikawa 923-1292, Japan
E-mail: d-yuchen@jaist.ac.jp

K. Uryu
Advantest Laboratories Ltd.
48-2 Matsubara, Kami-Ayashi, Aoba-ku, Sendai, Miyagi 989-3124, Japan

The ORCID identification number(s) for the author(s) of this article can be found under https://doi.org/10.1002/pssa.202500266.

DOI: 10.1002/pssa.202500266

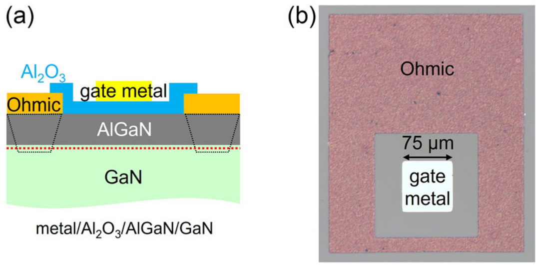

Figure 1. a) The schematic and b) the top view of the metal/Al_2O_3/AlGaN/GaN capacitor devices.

trimethyl aluminum and water. The Al_2O_3 thicknesses $d_{Al_2O_3}$ are 16, 22, and 28 nm, which were confirmed by ellipsometry measurements of reference samples obtained by side-by-side deposition. We completed the device fabrication by gate metal formation using a Ni film ≈5 nm covered by an Au film ≈100 nm, both obtained by vacuum evaporation. The top view of the fabricated devices is shown in **Figure** 1b.

For the fabricated metal/Al_2O_3/AlGaN/GaN MIS devices, the gate current densities J between the gates and the grounded Ohmic electrodes were measured in comparison with a metal/AlGaN/GaN Schottky device. **Figure 2** shows the measured J–V characteristics, J as a function of the gate voltage V_G. The gate leakage currents, both on forward and reverse biases, are effectively suppressed by the Al_2O_3 gate insulator, ensuring that the capacitance and conductance of the devices can be evaluated properly for $V_G \leq 7$ V. Moreover, we measured C–V characteristics between the gates and the grounded Ohmic electrodes of the MIS devices at frequency $f = 1$ MHz. **Figure 3** shows the measured capacitance C_{meas} as a function of the gate voltage V_G, as well as the 2D electron gas concentration n_s obtained by integrating the C–V characteristics using $C_{meas} = \partial(qn_s)/\partial V_G$. From the n_s–V characteristics, we find linear relations $qn_s \simeq C(V_G - V_{th})$, from which we can determine the threshold voltage V_{th} and C, where $1/C = 1/C_{Al_2O_3} + 1/C_{AlGaN} = d_{Al_2O_3}/(k_{Al_2O_3}\varepsilon_0) + 1/C_{AlGaN}$ using the insulator capacitance $C_{Al_2O_3}$, the AlGaN capacitance C_{AlGaN}, the insulator thickness $d_{Al_2O_3}$, and the insulator dielectric constant $k_{Al_2O_3}$. The inset of Figure 3 shows $1/C$ as a function of $d_{Al_2O_3}$. By linear fitting, we obtain $k_{Al_2O_3} \simeq 8$ from the slope, which

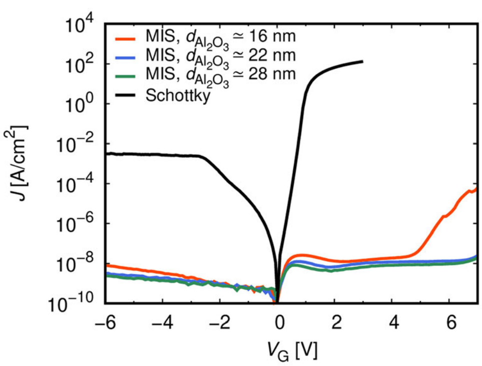

Figure 2. J–V characteristics of metal/Al_2O_3/AlGaN/GaN MIS devices, in comparison with those of a metal/AlGaN/GaN Schottky device.

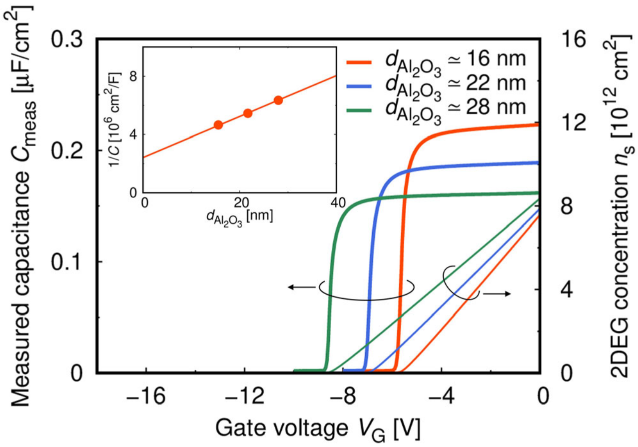

Figure 3. C–V and n_s–V characteristics of the metal/Al_2O_3/AlGaN/GaN MIS devices. Inset: $1/C$ as a function of $d_{Al_2O_3}$.

is a reasonable value for amorphous Al_2O_3. **Figure 4** shows the obtained V_{th} as a function of $d_{Al_2O_3}$, where we obtain a linear relation given by

$$V_{th} = \frac{\sigma_{GaN} - \sigma_{int}}{k_{Al_2O_3}\varepsilon_0} d_{Al_2O_3} + \text{const.} \tag{1}$$

using the GaN polarization charge density σ_{GaN} and the insulator–semiconductor interface fixed charge density σ_{int}. From the slope, we obtain $\sigma_{int}/q \simeq 3.2 \times 10^{13}$ cm^{-2} assuming $\sigma_{GaN}/q \simeq 2.1 \times 10^{13}$ cm^{-2},[37–41] as shown in the inset of Figure 4 in comparison with AlGaN polarization charge density σ_{AlGaN}, where the error bar stands for the three-sigma standard deviations of the linear fitting. This result indicates that the Al_2O_3/AlGaN interface is nearly neutral, being consistent with other studies.[23–27,31,42,43]

Furthermore, we investigated f-dependent C–V characteristics in order to examine the insulator(Al_2O_3)–semiconductor (AlGaN) interface trap densities of the devices. **Figure 5** shows an example of the measured f-dependent C–V characteristics for $d_{Al_2O_3} =$ 22 nm at frequency $f =$ 100 Hz-1 MHz, where we find that the devices exhibit very weak frequency dispersion of the C–V

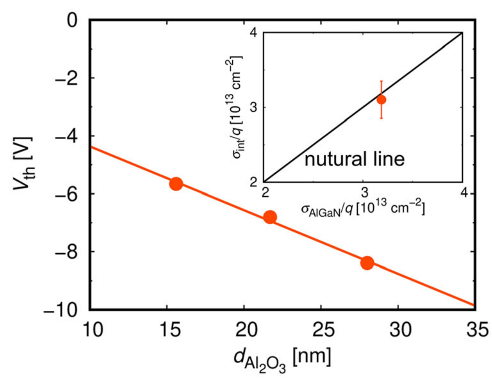

Figure 4. The threshold voltages V_{th} as a function of $d_{Al_2O_3}$. Inset: the interface fixed charge density σ_{int} in comparison with the AlGaN polarization charge density.

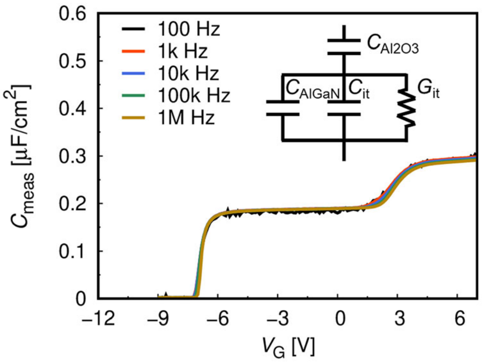

Figure 5. f-dependent C–V characteristics of the metal/Al_2O_3/AlGaN/GaN MIS device with $d_{Al_2O_3} = 22$ nm. Inset: the equivalent circuit.

characteristics. By using the conductance method, we evaluated the interface trap densities of the devices based on the circuit shown in the inset of Figure 5, which is a small signal equivalent circuit at a fixed bias voltage. To describe electron trapping (and also detrapping) by the interface trap level at the Fermi energy, the circuit includes the interface trap admittance (as a function of $\omega = 2\pi f$), whose real part is the trap conductance G_{it}, where

$$\frac{G_{it}}{\omega} = \frac{q^2 D_{it} \ln(1+\omega^2\tau^2)}{2\omega\tau} \tag{2}$$

and the imaginary part is $C_{it}\omega$, where

$$C_{it} = \frac{q^2 D_{it} \operatorname{atan}(\omega\tau)}{\omega\tau} \tag{3}$$

is the trap capacitance, using the trapping time constant τ of the trap level at the Fermi energy. It should be noted that, while generally the trap levels are continuously distributed in the semiconductor energy gap, at the fixed bias voltage, the corresponding trap level is specified by the Fermi energy position. According to Equation (2), usually G_{it}/ω exhibits a single-peaked behavior as a function of f, from which τ can be evaluated by the peak frequency $f_p = 1/(\pi\tau)$ and the interface trap density D_{it} by the peak value $G_{it}/\omega \simeq 0.4q^2 D_{it}$. **Figure 6**a shows the measured G_{it}/ω for several forward bias voltages, showing the single-peaked behavior and $D_{it} \approx 3 \times 10^{13}$ cm^{-2} eV^{-1}. Electron trapping and detrapping take place between the AlGaN conduction band and Al_2O_3/AlGaN interface trap level at the Fermi energy. With continuous increase in positive bias voltages, continuous increase in the peak frequency of G_{it}/ω is observed, corresponding to decrease in the energy difference between the AlGaN conduction band bottom E_C and the Fermi energy E_F of the AlGaN/GaN, indicating that the AlGaN layer is depleted and plays the role of the depletion layer. The time constant τ is given by

$$\tau = \tau_0 e^{(E_C - E_F)/k_B T} \tag{4}$$

where $\tau_0 \propto 1/\sigma_e$ is a time constant inversely proportional to the electron capture cross section σ_e of the trap. Even though τ_0 is ambiguous due to the uncertainty of σ_e, by assuming a wide range of $\tau_0 \approx 0.1$–1000 ps, we can estimate the "activation energy" E_C–$E_F \approx 0.6$ eV from the evaluated τ. Figure 6b shows D_{it} as a function of E_C–E_F, with horizontal and vertical error bars corresponding to the wide-range τ_0 and the three-sigma asymptotic standard errors of the fittings using Equation (2), respectively. Based on this, we obtain the band diagram of the metal/Al_2O_3/AlGaN/GaN MIS devices by Poisson–Schrödinger calculation. The inset of Figure 6b shows the band diagram for $V_G = 7$ V. At this bias voltage, owing to the high $D_{it} \approx 3 \times 10^{13}$ cm^{-2} eV^{-1}, high-density electrons are admitted at the Al_2O_3/AlGaN interface, and the AlGaN layer stays to be depleted, leading to electron trapping and detrapping between the AlGaN conduction band and the Al_2O_3/AlGaN interface trap level at E_F.

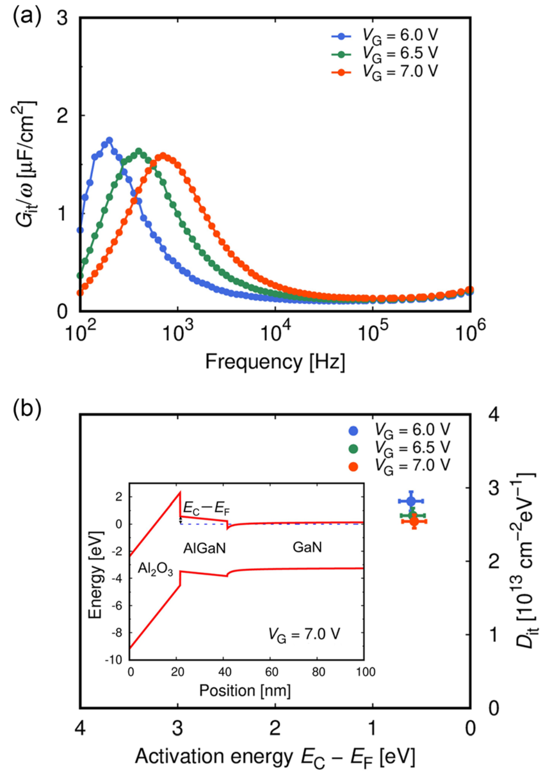

Figure 6. a) G_{it}/ω as functions of frequency for the metal/Al_2O_3/AlGaN/GaN MIS device with $d_{Al_2O_3} = 22$ nm. b) The interface trap density D_{it} as a function of the activation energy E_C–E_F. Inset: the band diagram obtained by Poisson–Schrödinger calculation for $V_G = 7$ V.

It should be noted that, while the interface trap density for the device is rather high over 10^{13} cm^{-2} eV^{-1}, the frequency dispersion of the C–V characteristics is very weak. This implies that very weak C–V frequency dispersion is not necessarily associated with a low interface trap density. On the other hand, tails of G_{it}/ω are observed, slightly increasing at $\lesssim$1 MHz. These tails are specific to the present gate insulator; different gate insulators exhibit no tails.[4,35] Thus, it is suggested that, for the present gate insulator, a second peak may exist at a higher frequency.

3. Double-Peak Model

As a possible explanation for the weak C–V frequency dispersion despite the high D_{it}, we consider a double-peak model,[44–47] whose equivalent circuit is shown in **Figure 7**. In this model,

G_{it} and C_{it} are parallel connections of two components, corresponding to two different types of traps, with trap densities D_{it1} and D_{it2}, and distinct trapping time constants τ_1 and τ_2.[48,49] In fact, two clear peaks at the frequencies of ≈1 kHz and 10 MHz ranges have been observed, corresponding to long and short trapping time constants, respectively.[45,47] This model assumes that there are two types of continuously distributed traps, and thus, two degenerate trap levels at the Fermi energy determined by the fixed bias voltage. The two trap levels have the same activation energy E_C–E_F, but different trap densities and also different trapping time constants owing to different $\tau_0 \propto 1/\sigma_e$. The circuit is, thus, described by

$$\frac{G_{it}}{\omega} = \frac{q^2 D_{it1} \ln(1+\omega^2{\tau_1}^2)}{2\omega\tau_1} + \frac{q^2 D_{it2} \ln(1+\omega^2{\tau_2}^2)}{2\omega\tau_2} \tag{5}$$

and

$$C_{it} = \frac{q^2 D_{it1} \operatorname{atan}(\omega\tau_1)}{\omega\tau_1} + \frac{q^2 D_{it2} \operatorname{atan}(\omega\tau_2)}{\omega\tau_2} \tag{6}$$

As a result, G_{it}/ω exhibits a double-peaked behavior as a function of f.

By a model calculation, let us see the behavior of the double-peak model in comparison with the single-peak model, where the latter does not include the second terms of Equation (5) and (6). Assuming $C_{Al_2O_3} = 300\,\text{nF cm}^{-2}$, $C_{AlGaN} = 400\,\text{nF cm}^{-2}$, $D_{it1} = 2.5\times10^{13}\,\text{cm}^{-2}\,\text{eV}^{-1}$, $\tau_1 = 10^{-4}$ s, $D_{it2} = 3.0\times10^{13}\,\text{cm}^{-2}\,\text{eV}^{-1}$, and $\tau_2 = 10^{-8}$ s, we calculated G_{it}/ω and C_{it} as functions of frequency for the double-peak model. For comparison, G_{it}/ω and C_{it} for the single-peak model without the second terms of Equation (5) and (6) are also calculated. **Figure 8**a shows the calculated G_{it}/ω for both models, where a single- or double-peaked behavior can be observed. For relatively low frequency $\lesssim 1$ MHz, we observe similar behavior of G_{it}/ω for both the single- and double-peak models. However, for relatively high frequency $\gtrsim 1$ MHz, a second peak of G_{it}/ω exists for the double-peak model, while G_{it}/ω vanishes for the single-peak model. Figure 8b shows the calculated C_{it} for both models. While the variation of C_{it} is from 0 to $\approx 4\,\mu\text{F cm}^{-2}$ for the single-peak model, the double-peak model always exhibits C_{it} larger than $\approx\mu\text{F cm}^{-2}$ order. This different behavior of C_{it} will lead to different frequency dispersion of the measured capacitance C_{meas}. **Figure 9** shows the calculated prediction of the measured capacitance C_{meas} as a function of frequency, based on the single- and double-peak models. For the single-peak model, at frequency $\lesssim 100$ kHz, C_{it} is large (larger than $\approx\mu\text{F cm}^{-2}$ order), and thus, C_{meas} will be similar to the capacitance of the gate insulator $C_{meas} = C_{Al_2O_3}(C_{AlGaN} + C_{it})/(C_{Al_2O_3} + C_{AlGaN} + C_{it}) \simeq C_{Al_2O_3}$. When the frequency increases, the vanishing C_{it} leads to

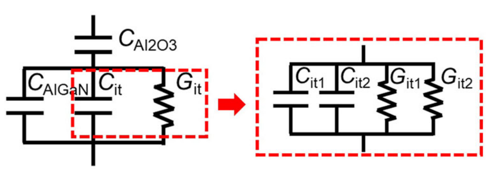

Figure 7. The equivalent circuit for the double-peak model.[44–47]

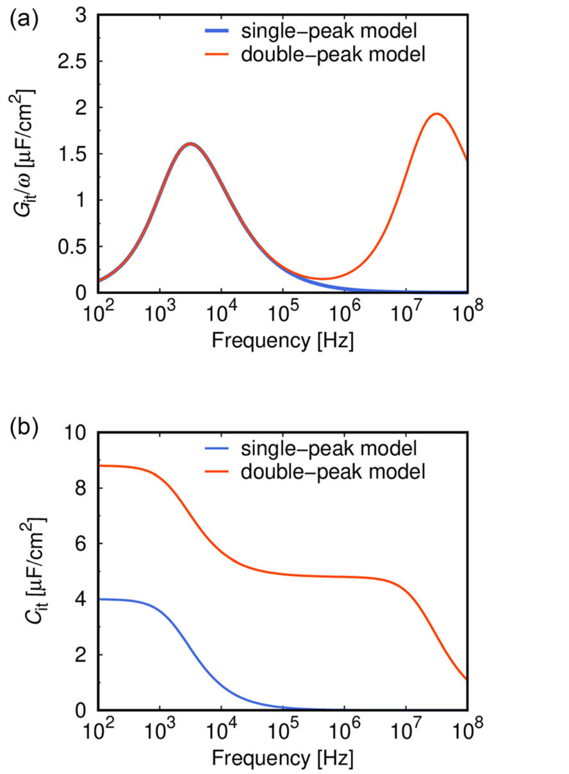

Figure 8. a) G_{it}/ω and b) C_{it} as functions of frequency obtained by the single- and double-peak models. We assume $C_{Al_2O_3} = 300\,\text{nF cm}^{-2}$, $C_{AlGaN} = 400\,\text{nF cm}^{-2}$, $D_{it1} = 2.5\times10^{13}\,\text{cm}^{-2}\,\text{eV}^{-1}$, $\tau_1 = 10^{-4}$ s, $D_{it2} = 3.0\times10^{13}\,\text{cm}^{-2}\,\text{eV}^{-1}$, and $\tau_2 = 10^{-8}$ s.

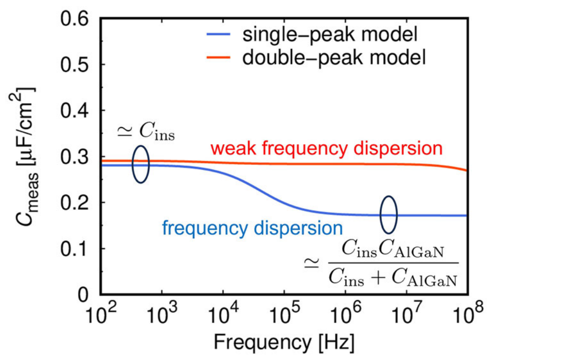

Figure 9. The calculated prediction of the measured capacitance C_{meas} as a function of frequency based on the single- and double-peak models.

$C_{meas} \simeq C_{Al_2O_3}C_{AlGaN}/(C_{Al_2O_3} + C_{AlGaN})$. As a result, frequency dispersion can be observed around the frequency ≈10 kHz–100 kHz for the single-peak model. On the other hand, since C_{it} is larger than $\approx\mu\text{F cm}^{-2}$ order up to 10^8 Hz for the double-peak model, C_{meas} will remain to be $C_{meas} = C_{Al_2O_3}(C_{AlGaN} + C_{it})/(C_{Al_2O_3} + C_{AlGaN} + C_{it}) \simeq C_{Al_2O_3}$. This leads to very weak frequency dispersion of C_{meas} for the double-peak model, despite the assumed high interface trap densities over $10^{13}\,\text{cm}^{-2}\,\text{eV}^{-1}$. These results at least show that there is a case where a MIS device exhibits very weak C–V frequency dispersion even with a high interface trap density, and therefore an apparent weak C–V frequency dispersion does not necessarily indicate a low interface trap density.

The double-peak model is applied to the measurement results shown in the previous section, in comparison with the single-peak model. **Figure 10** shows the measured G_{it}/ω for the metal/Al_2O_3/AlGaN/GaN MIS device, fitted by the single- or double-peak model. Both models well describe the observed peak at ≈kHz. On the other hand, around ≲1 MHz, there exists a tail of a second peak of G_{it}/ω in the measurement results, with a peak frequency higher than the measurement frequency range, suggesting the existence of another kind of traps with a rather short trapping time constant $\approx 10^{-8}$ s. This tail of the second peak can be described only by the double-peak model. **Figure 11** shows the measured capacitance C_{meas} of the device as a function of frequency, in comparison to the calculation by single- or double-peak model, shown by dotted and solid lines, respectively. The double-peak model well explains the weak frequency dispersion of C_{meas} in the measurement frequency range. The interface traps significantly depend on the device fabrication processes and the insulator quality. For the present devices, owing to the fact that the double-peak model explains the experimental results well, we assume two types of traps, including the one that has a short trapping time constant corresponding to the second peak. Although it is difficult to clarify the origin of the traps, it should be noted that the trapping time constant is given by $\tau_0 \propto 1/\sigma_e$, inversely proportional to the capture cross section of the traps. Thus, in the present devices, it is plausible to assume that there exist traps with a rather large capture cross section.

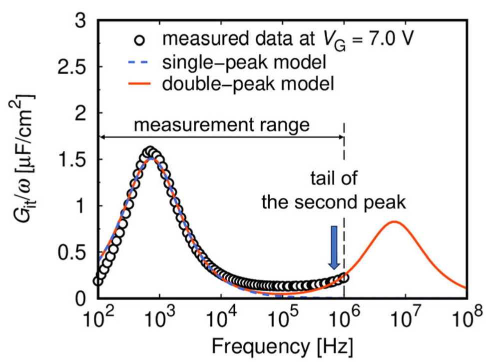

Figure 10. Measured G_{it}/ω in comparison with calculated curves obtained by the single- and double-peak models.

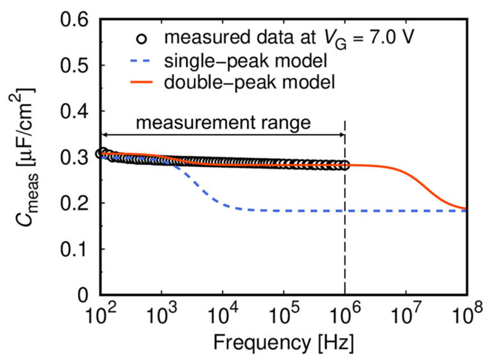

Figure 11. Measured capacitance C_{meas} in comparison with calculated curves obtained by the single- and double-peak models.

4. Conclusion

We fabricated metal/Al_2O_3/AlGaN/GaN MIS devices and evaluated the interface trap density by the conductance method. We found a rather high interface trap density $\approx 3 \times 10^{13}$ cm^{-2} eV^{-1}, even though we observed very weak frequency dispersion of the C–V characteristics. As a possible explanation, we consider a double-peak model, which includes two different types of traps with distinct trapping time constants. The model underlines the possibility that a high interface trap density does not necessarily lead to strong C–V frequency dispersion. This implies that it is not appropriate to naively discuss the trap density just by apparent C–V frequency dispersion.

Acknowledgements

This work was supported by JSPS KAKENHI (grant nos. JP22H01545 and JP23K22815).

Conflict of Interest

The authors declare no conflict of interest.

Data Availability Statement

The data that support the findings of this study are available from the corresponding author upon reasonable request.

Keywords

AlGaN/GaN device, frequency dispersion, interface trap

Received: March 25, 2025
Revised: May 2, 2025
Published online: June 8, 2025

[1] T. Hashizume, S. Ootomo, H. Hasegawa, *Appl. Phys. Lett.* **2003**, *83*, 2952.
[2] S. P. Le, T. Ui, T. Q. Nguyen, H. A. Shih, T. Suzuki, *J. Appl. Phys.* **2016**, *119*, 204503.
[3] A. Colon, L. Stan, R. Divan, J. Shi, *J. Vac. Sci. Technol. A* **2017**, *35*, 01B132.
[4] S. P. Le, D. D. Nguyen, T. Suzuki, *J. Appl. Phys.* **2018**, *123*, 034504.
[5] S. Dutta Gupta, A. Soni, V. Joshi, J. Kumar, R. Sengupta, H. Khand, B. Shankar, N. Mohan, S. Raghavan, N. Bhat, M. Shrivastava, *IEEE Trans. Electron Devices* **2019**, *66*, 2544.
[6] D. D. Nguyen, T. Suzuki, *J. Appl. Phys.* **2020**, *127*, 094501.
[7] D. D. Nguyen, T. Isoda, Y. Deng, T. Suzuki, *J. Appl. Phys.* **2021**, *130*, 014503.
[8] D. D. Nguyen, Y. Deng, T. Suzuki, *Semicond. Sci. Technol.* **2023**, *38*, 095010.

[9] C. Gupta, S. H. Chan, A. Agarwal, N. Hatui, S. Keller, U. K. Mishra, *IEEE Electron Device Lett.* **2017**, *38*, 1575.
[10] D. Kikuta, K. Ito, T. Narita, T. Kachi, *Appl. Phys. Express* **2020**, *13*, 026504.
[11] C. Liu, E. F. Chor, L. S. Tan, *Appl. Phys. Lett.* **2006**, *88*, 173504.
[12] A. Kawano, S. Kishimoto, Y. Ohno, K. Maezawa, T. Mizutani, H. Ueno, T. Ueda, T. Tanaka, *Phys. Status Solidi C* **2007**, *4*, 2700.
[13] S. Yagi, M. Shimizu, M. Inada, Y. Yamamoto, G. Piao, H. Okumura, Y. Yano, N. Akutsu, H. Ohashi, *Solid-State Electron.* **2006**, *50*, 1057.
[14] T. Sato, J. Okayasu, M. Takikawa, T. Suzuki, *IEEE Electron Device Lett.* **2013**, *34*, 375.
[15] M. Nozaki, K. Watanabe, T. Yamada, H. A. Shih, S. Nakazawa, Y. Anda, T. Ueda, A. Yoshigoe, T. Hosoi, T. Shimura, H. Watanabe, *Jpn. J. Appl. Phys.* **2018**, *57*, 06KA02.
[16] Y. Liu, J. Bardwell, S. McAlister, S. Rolfe, H. Tang, J. Webb, *Phys. Status Solidi C* **2003**, *1*, 69.
[17] H. A. Shih, M. Kudo, M. Akabori, T. Suzuki, *Jpn. J. Appl. Phys.* **2012**, *51*, 02BF01.
[18] H. A. Shih, M. Kudo, T. Suzuki, *Appl. Phys. Lett.* **2012**, *101*, 043501.
[19] H. A. Shih, M. Kudo, T. Suzuki, *J. Appl. Phys.* **2014**, *116*, 184507.
[20] S. P. Le, T. Q. Nguyen, H. A. Shih, M. Kudo, T. Suzuki, *J. Appl. Phys.* **2014**, *116*, 054510.
[21] J. C. Gerbedoen, A. Soltani, M. Mattalah, M. Moreau, P. Thevenin, J. C. D. Jaeger, *Diamond Relat. Mater.* **2009**, *18*, 1039.
[22] T. Q. Nguyen, H. A. Shih, M. Kudo, T. Suzuki, *Phys. Status Solidi C* **2013**, *10*, 1401.
[23] S. Ganguly, J. Verma, G. Li, T. Zimmermann, H. Xing, D. Jena, *Appl. Phys. Lett.* **2011**, *99*, 193504.
[24] M. Esposto, S. Krishnamoorthy, D. N. Nath, S. Bajaj, T.-H. Hung, S. Rajan, *Appl. Phys. Lett.* **2011**, *99*, 133503.
[25] M. Ťapajna, J. Kuzmík, *Appl. Phys. Lett.* **2012**, *100*, 113509.
[26] J. Son, V. Chobpattana, B. M. McSkimming, S. Stemmer, *Appl. Phys. Lett.* **2012**, *101*, 102905.
[27] T. H. Hung, S. Krishnamoorthy, M. Esposto, D. N. Nath, P. S. Park, S. Rajan, *Appl. Phys. Lett.* **2013**, *102*, 072105.
[28] J. T. Asubar, Z. Yatabe, D. Gregusova, T. Hashizume, *J. Appl. Phys.* **2021**, *129*, 121102.
[29] E. H. Nicollian, J. R. Brews, *MOS (Metal Oxide Semiconductor) Physics and Technology*, John Wiley & Sons, Hoboken, New Jersey **2002**.
[30] Y. Hori, Z. Yatabe, T. Hashizume, *J. Appl. Phys.* **2013**, *114*, 244503.
[31] M. Ťapajna, M. Jurkovič, L. Válik, Š. Haščík, D. Gregušová, F. Brunner, E.-M. Cho, T. Hashizume, J. Kuzmík, *J. Appl. Phys.* **2014**, *116*, 104501.
[32] Z. Zhang, M. Hua, J. He, G. Tang, Q. Qian, K. J. Chen, *Appl. Phys. Express* **2018**, *11*, 081003.
[33] A. Calzolaro, N. Szabó, A. Großer, J. Gärtner, T. Mikolajick, A. Wachowiak, *Phys. Status Solidi A* **2021**, *218*, 2000585.
[34] T. Hashizume, K. Nishiguchi, S. Kaneki, J. Kuzmik, Z. Yatabe, *Mater. Sci. Semicond. Process* **2018**, *78*, 85.
[35] Y. Deng, J. Gelan, K. Uryu, T. Suzuki, *J. Appl. Phys.* **2024**, *135*, 084504.
[36] Y. Deng, J. Gelan, K. Uryu, T. Suzuki, in *2024 Inter. Conf. on Solid State Devices and Materials*, D-7-02 (**2024**).
[37] J. Garrido, J. Sanchez Rojas, A. Jimenez, E. Munoz, F. Omnes, P. Gibart, *Appl. Phys. Lett.* **1999**, *75*, 2407.
[38] O. Ambacher, B. Foutz, J. Smart, J. R. Shealy, N. G. Weimann, K. Chu, M. Murphy, A. J. Sierakowski, W. J. Schaff, L. F. Eastman, R. Dimitrov, A. Mitchell, M. Stutzmann, *J. Appl. Phys.* **2000**, *87*, 334.
[39] F. Bernardini, V. Fiorentini, D. Vanderbilt, *Phys. Rev. B* **2001**, *63*, 193201.
[40] E. Miller, E. Yu, C. Poblenz, C. Elsass, J. Speck, *Appl. Phys. Lett.* **2002**, *80*, 3551.
[41] A. Winzer, R. Goldhahn, G. Gobsch, A. Link, M. Eickhoff, U. Rossow, A. Hangleiter, *Appl. Phys. Lett.* **2005**, *86*, 181912.
[42] M. Matys, B. Adamowicz, A. Domanowska, A. Michalewicz, R. Stoklas, M. Akazawa, Z. Yatabe, T. Hashizume, *J. Appl. Phys.* **2016**, *120*, 225305.
[43] M. Ťapajna, L. Válik, F. Gucmann, D. Gregušová, K. Frohlich, Š. Haščík, E. Dobročka, L. Tóth, B. Pécz, J. Kuzmík, *Vac. Sci. Technol. B* **2017**, *35*, 01A107.
[44] S. Kumar, P. Gupta, I. Guiney, C. J. Humphreys, S. Raghavan, R. Muralidharan, D. N. Nath, *IEEE Trans. Electron Devices* **2017**, *64*, 4868.
[45] M. Whiteside, S. Arulkumaran, Y. Dikme, A. Sandupatla, G. Ng, *Mater. Sci. Eng. B* **2020**, *262*, 114707.
[46] M. Whiteside, S. Arulkumaran, G. I. Ng, *Mater. Sci. Eng. B* **2021**, *270*, 115224.
[47] P. Dalapati, S. Arulkumaran, D. Mani, H. Li, H. Xie, Y. Wang, G. I. Ng, *Mater. Sci. Eng. B* **2024**, *307*, 117503.
[48] X. Lu, K. Yu, H. Jiang, A. Zhang, K. M. Lau, *IEEE Trans. Electron Devices* **2017**, *64*, 824.
[49] Q. Wang, X. Cheng, L. Zheng, L. Shen, J. Li, D. Zhang, R. Qian, Y. Yu, *RSC Adv.* **2017**, *7*, 11745.

